Advanced Functional Materials

ADVANCED FUNCTIONAL MATERIALS
www.afm-journal.de

RESEARCH ARTICLE

Heterogeneous Coherent Interface Enabling Nonstochastic Crystallization for Phase-Change Memory

Tian-Yu Zhao[1] | Jiahao Li[2] | Nian-Ke Chen[1] | Bai-Qian Wang[1] | Xiaomin Cheng[2] | Shun-Yao Qin[1] | Huan-Ran Ding[1] | Shengbai Zhang[3] | Hong-Bo Sun[4] | Xiangshui Miao[2] | Xian-Bin Li[1]

[1]State Key Laboratory of Integrated Optoelectronics, College of Electronic Science and Engineering (College of Integrated Circuits), Jilin University, Changchun, China | [2]School of Integrated Circuits, Hubei Key Laboratory for Advanced Memories, Wuhan National Laboratory for Optoelectronics, Huazhong University of Science and Technology, Wuhan, China | [3]Department of Physics, Applied Physics, and Astronomy, Rensselaer Polytechnic Institute, Troy, New York, USA | [4]State Key Lab of Precision Measurement Technology and Instruments, Department of Precision Instrument, Tsinghua University, Beijing, China

Correspondence: Nian-Ke Chen (chennianke@jlu.edu.cn) | Xiaomin Cheng (xmcheng@hust.edu.cn) | Xiangshui Miao (miaoxs@hust.edu.cn) | Xian-Bin Li (lixianbin@jlu.edu.cn)

Received: 2 September 2025 | **Revised:** 17 January 2026 | **Accepted:** 18 January 2026

Keywords: coherent interface | high-throughput material screening | nonstochastic crystallization | phase-change memory materials

ABSTRACT

Phase-change memory (PCM) displays great promise for the storage-class memory (SCM) technology due to its combination of fast speed of dynamic random-access memory and nonvolatility of Flash. Yet, to meet the high industrial requirement of write/erase speed for the SCM application, robust strategies for further accelerating phase transition, particularly from amorphous to crystalline PCM materials, are urgently needed. In this work, we propose a unique strategy of coherent-interface induced ultrafast crystallization in PCM materials. Employing rock-salt YAs/$Ge_2Sb_2Te_5$ as a prototype, systematic first-principles molecular dynamics demonstrate that rapid nonstochastic crystallization behaviors can be achieved by the rock-salt-lattice-matching and high-temperature-resistant heterogeneous interface attached to the popular PCM material $Ge_2Sb_2Te_5$ (GST). Further experiment shows that the YAs-incorporated GST device has a faster SET process compared with the pure GST device. Finally, to extend the strategy in the family of inorganic materials, high-throughput screening from over 150 000 structures discovers as many as 71 candidates for coherent interfaces with PCM GST. The present study establishes a promising strategy to overcome the speed bottleneck of PCM through atomic-scale interface design for future storage-class memory implementation.

1 | Introduction

Phase-change memory (PCM) is a prospective candidate for storage-class memory (SCM) [1–6], which holds promise for resolving the substantial computational demands in emerging fields such as generative AI models, machine learning force field molecular dynamics, and advanced autonomous driving technologies. The exceptional write/erase speed of PCM positions it as a potential complement to main memory in computing systems, such as dynamic random-access memory (DRAM) and static random-access memory (SRAM) [7–10]. Furthermore, its nonvolatile nature, good cycling endurance, and excellent data retention are comparable to existing external storage devices (e.g., NAND Flash) [11–18]. These attributes endow PCM with the potential to serve as storage-class memory, which can reshape complex and hierarchical data storage architectures designed to balance performance and cost, thereby achieving a more efficient computing framework [3]. Since 2015, Intel and Micron

Tian-Yu Zhao and Jiahao Li contributed equally to this work.

have successively released a series of PCM-based nonvolatile memory solutions (Intel Optane Solid-State Drive / Persistent Memory) [19, 20], with their speed up to 1000 times faster than Flash memory and data storage density 10 times greater than DRAM [11, 21]. However, the fundamental write-speed requirement for memory-type storage-class memory must be faster than 50 ns [3], whereas commercial PCM devices still exhibit a write speed of around 100 ns [21, 22], which poses a significant obstacle to the application of phase-change memory devices.

In the state-of-the-art $Ge_2Sb_2Te_5$ (GST)-based phase-change memory devices, the SET process (crystallization of amorphous GST materials into the rock-salt structured crystalline phase to achieve "0"–"1" signal transition) necessitates a prolonged voltage, which imposes the performance bottleneck in the write/erase time of the PCM technology. From the microscopic perspective, the crystallization of amorphous GST materials is a stochastic nucleation-driven process mediated by thermal fluctuations [23–26]. Specifically, at an appropriate temperature between the glass-transition temperature (T_g) and melting point (T_m), the crystallization of amorphous GST mainly starts from crystal nuclei that form randomly in the materials after a long incubation period [8, 27]. Previous ab initio molecular dynamics (AIMD) results have revealed that the formation of stable nuclei during the incubation period is the critical step in the crystallization of GST and can account for the majority of the total crystallization time [28, 29]. Also, the uncertainty caused by the stochastic nucleation is an important challenge in further optimizing the SET speed of PCM devices, especially in advanced miniaturized memory cells [8].

Many efforts have been made to reduce the crystallization time through various approaches. The pre-programming method, or pre-structural ordering method [28], employed a weak but consistent incubation voltage to increase the number of fourfold rings and distorted octahedral structures, which are believed to be the precursors of crystalline GST [30], in the materials and achieved subsequent rapid crystallization. Recognizing the high bonding strength and stability of the M-Te 6-coordinate octahedral structure (M refers to Sc [8, 31], Ti [32, 33], In [34, 35], etc.), researchers alloyed these elements with basic Ge-Sb-Te materials. This strategy effectively facilitated the formation and enhanced the stabilization of crystal nuclei, thereby realizing increases in crystallization speed to various extents. Some researchers concentrated on novel structures of $[(GeTe)_x/(Sb_2Te_3)_y]_n$ superlattices and successfully leveraged them for more rapid and energy-efficient transition between two states with distinct resistance [36–40]. Recently, introducing heterogeneous van der Waals (vdW) sublayers, such as $TiTe_2$ [41] and $HfTe_2$ [42], into PCM materials has been investigated to modulate the electrical and thermal properties and phase-change behaviors, consequently improving the overall performance of the devices [43]. Replacing the traditional SiO_2 dielectric materials with TiO_2 was also proposed to introduce the heterogeneous structure and improve SET speed [44]. These studies have made significant contributions to addressing this bottleneck in PCM devices and provided valuable insights. Nevertheless, with the escalating demand for further optimizing the performance of devices, especially for the promising SCM application, there still remains a strong need for new strategies that demonstrate clear microscopic mechanisms, exhibit higher robustness in accelerating SET speed, and hold broad potential for further exploration.

In this work, we present a novel strategy of nonstochastic ultrafast crystallization of PCM materials. The core of our approach lies in specific crystalline materials with structural compatibility to the popular PCM material GST, enabling the embedding of coherent interfaces directly into the memory cell. Utilizing the rock-salt-lattice-matching and high-temperature-resistant Yttrium Arsenide (YAs) as an example to construct a coherent interface with GST, first-principles molecular dynamics reveal nonstochastic crystallization behaviors in GST, resulting in significantly accelerated crystallization. Further experiments based on two kinds of PCM devices with 250 nm diameter holes filled by YAs-incorporated GST and pure GST, respectively, demonstrate that the YAs-incorporated GST device has a faster SET process compared with the pure GST device. Finally, by using four rational criteria (including rock-salt type structure, thermodynamic stability, small lattice mismatch, and high melting point), 71 potential candidates with the ability to form coherent interfaces with GST are selected using high-throughput screening analyses from more than 150 000 structures in the inorganic material family. We expect the present work to provide a robust strategy for speeding up crystallization in PCM materials via precise coherent interface design, with a promise for future storage-class memory applications.

2 | Results and Discussion

2.1 | Theoretical Design of the Coherent Interface

A coherent interface refers to a special interface where two crystalline materials match perfectly so that the two lattices are continuous across the interface [45]. Coherent interfaces have been employed to generate plastic deformability of silicon nitride ceramics [46] and design high-entropy alloys with comprehensive mechanical and magnetic performances [47]. However, in PCM devices, coherent interfaces are almost unexplored and should be designed to facilitate recrystallization. First, the candidate materials to construct hetero-coherent interfaces with PCM material should have a rock-salt structure consistent with crystalline PCM materials, such as the prototypical rock-salt $Ge_2Sb_2Te_5$ (GST). Second, the candidate materials should have a lattice constant well close to the PCM materials to allow the construction of coherent interfaces. Finally, the candidate materials should have good thermal stability to withstand the melt-quenching process during the RESET operations.

Taking GST as an example of the target PCM material, we choose YAs to demonstrate the concept of coherent interfaces in PCM devices. Since the 1960s, when YAs was reported along with other rare earth arsenides [48], it has still not attracted widespread interest from academia or industry. However, we have identified the rock-salt structure and other advantages of YAs, which not only meet the multiple requirements of the coherent interface construction, but also offer opportunities to unlock its application. The lattice constants of rock-salt YAs and GST are very close, at 5.83 and 6.07 Å, respectively, with a lattice mismatch of only 4%. These properties make it possible for a coherent interface structure in which the cation and anion sublattices on

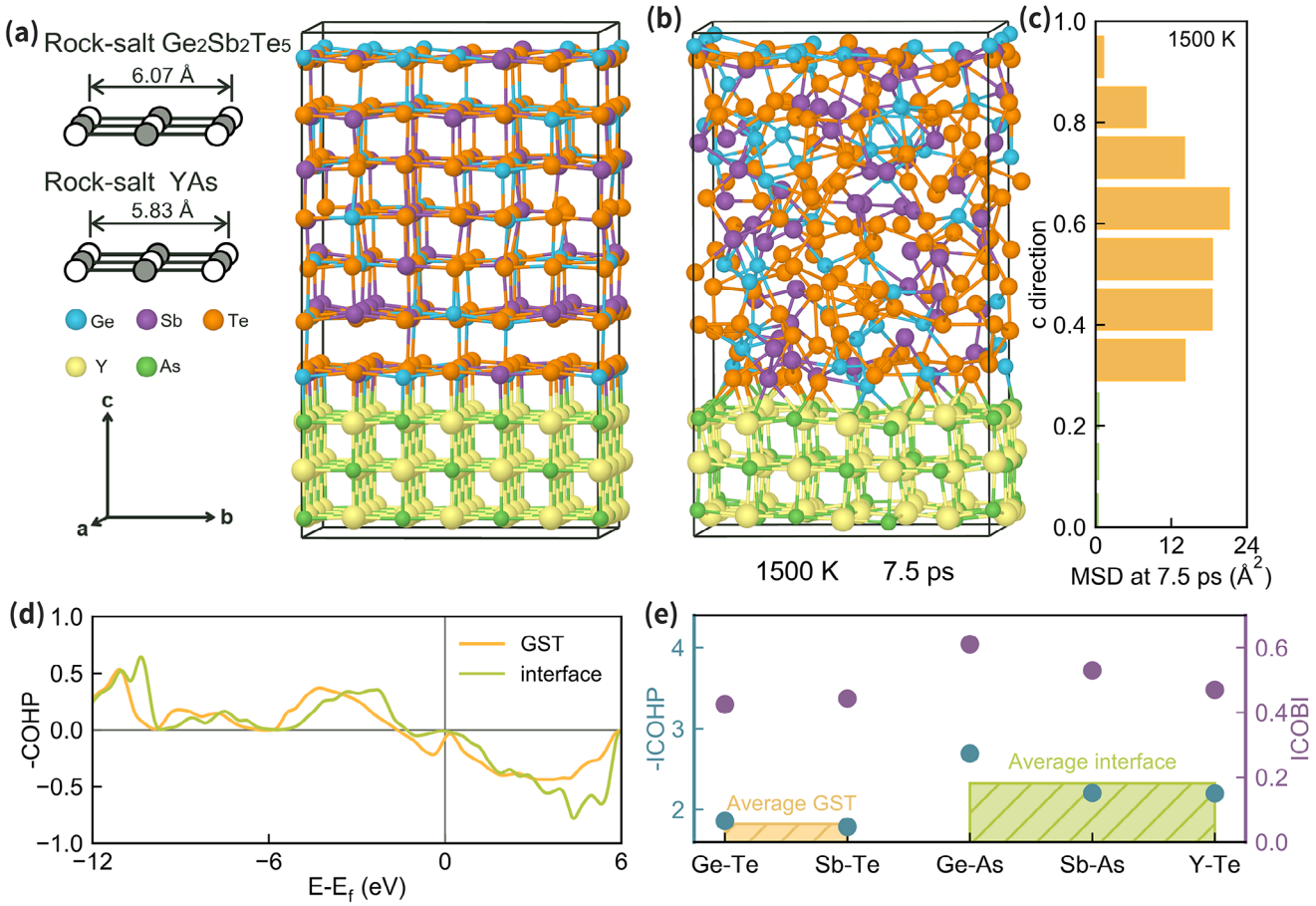

FIGURE 1 | Feasibility, stability, and bonding analysis of YAs-$Ge_2Sb_2Te_5$ (YAs-GST) coherent interface structure. (a) Lattice constants of rock-salt YAs and rock-salt GST, and the snapshot of the interface atomic structure. (b) YAs-GST interface structure after a 7.5-ps MD at 1500 K. (c) MSD of atoms in different regions across the c direction. (d) Average COHP at the interface (including Ge—As, Sb—As, and Y—Te) and within the GST part (including Ge—Te and Sb—Te). (e) ICOHP and ICOBI of different bonds in detail. The green and orange bars represent the average ICOHP at the interface and within the GST part, respectively.

both sides of the interface are compatible, forming Y—Te and Ge/Sb—As bonds at the interface, as depicted in Figure 1a. YAs also possesses a high melting point (2733 K predicted by the GNN model [49], note that its melting point is still unreported in previous experiments). Since the melting point of GST is 900 K [50], the RESET operation of the PCM device will not be strong enough to melt YAs. Next, the thermal stability of YAs in the coherent interface structure is investigated by first-principles molecular dynamics (MD). After heating the interface structure of Figure 1a to a high temperature of 1500 K for 7.5 ps, GST indeed turns to a disordered state while YAs still retains the ordered crystalline structure, showing no evidence of atomic diffusion between GST and YAs, as displayed in Figure 1b. Figure 1c further presents the mean square displacement (MSD) of atoms at 7.5 ps in different regions along the *c*-direction to quantitatively evaluate the degree of atomic diffusion. The atomic diffusions of YAs are negligible (manifested by very small MSDs) while those of GST are more significant, further confirming the high stability of YAs. On the other hand, in the GST region, atoms near the YAs interface manifest lower average displacement compared to those in the central region, suggesting the strong bonding effect between YAs and GST.

Further, we carry out in-depth calculations and analyses of the bonding nature at the interface. Figure 1d shows the average crystal orbital Hamilton population (COHP) at the interface (including Ge—As, Sb—As, and Y—Te bonds) and the average COHP in the GST region (including Ge—Te and Sb—Te bonds) in the crystalline interface structure of Figure 1a. As a powerful method, COHP enables us to analyze the bonding (−COHP > 0) and antibonding (−COHP < 0) energy regions of chemical bonding in materials [51]. Here, the COHP of GST exhibits pronounced antibonding states below the Fermi level, consistent with the previous report [52]. In contrast, the average COHP at the interface shows significantly reduced antibonding states in the same range. These findings once again indicate stronger bonding at the interface than inside GST. To quantify the bonding strength and covalency in the YAs/GST coherent interface, the integrated COHP (ICOHP) below the Fermi level and the integrated crystal orbital bond index (ICOBI) of different chemical bonds in the structure in Figure 1a are also calculated, as shown in Figure 1e. Specifically, ICOBI extends the traditional bond index concepts in chemistry to crystalline materials, thus enabling us to analyze the covalency of bonding in the structure [53]. The results reveal that the three types of chemical bonds at the interface (Ge—As, Sb—As,

and Y—Te) generally exhibit greater covalency (larger ICOBI values) and higher bonding strength (larger −ICOHP values) than those within the GST region, with the Ge—As bond standing out as the most robust. The charge density differences are shown in Figure S1, which also demonstrate strong bonding effect at the interface. The high thermal stability of YAs and relatively strong interface bonding between YAs and GST collectively demonstrate the great potential of the coherent interface to serve as a robust crystallization template in amorphous GST materials.

2.2 | Coherent Interfaces Enabled Nonstochastic and Fast Crystallization

To further verify the effect of the YAs/GST coherent interface on the crystallization behavior of GST materials, we perform first-principles molecular dynamics (MD) simulations of the recrystallization process. The amorphous GST interface structure is obtained by the melt-quenching method, with details in Section 4. The recrystallization is simulated by annealing the model at 600 K. The same simulation using the pure GST model (bulk-GST) without the coherent interface is also performed for comparison.

Figure 2a,b depicts the time evolutions of the pair correlation function of GST in the two models. The YAs-GST exhibits good ordering as early as 105 ps, accompanied by the remarkable increases of the peaks at 3, 4.2, 6.7, and 9.3 Å. Also, the emergence of a subtle peak at 5.3 Å can be observed. In contrast, the bulk GST material does not show significantly discernible crystalline characteristics during the initial 300 ps. Figure 2c compares the time evolutions of fourfold rings in GST, which has been regarded as an indicator of the crystallinity [30, 54] for PCM materials, during the two simulations. The crystallization process is divided into three stages: Stage I corresponds to the incubation period, Stage II to the crystallization development period, and Stage III to the slow-evolution period. For the pure GST, the model undergoes a longer incubation period of approximately 300 ps (Stage I), followed by the crystallization process (Stage II). During the incubation period, the number of fourfold rings fluctuates over time, indicating the frequent formation and dissolution of small crystal nuclei or crystal precursors. The detailed GST structures in the crystallization process are provided in Figure S2. On the contrary, the YAs-GST model with the coherent interface experiences a rapid and sharp increase in fourfold rings after a very brief period (within 10 ps), and then achieves a complete crystallization by 105 ps. The insets in Figure 2c show the key snapshots of the structures during the simulations, further confirming the conclusions. Obviously, the most remarkable improvement of the coherent interface is the shortening of the incubation time (Stage I). As predicted, the coherent interface serves as the template for crystallization and thus bypasses the incubation process, which is usually a stochastic process. In other words, the coherent interface will significantly improve the SET speed of PCM devices owing to the nonstochastic recrystallization process.

The role of YAs as the crystallization template can also be directly inferred from the structural characteristics of amorphous GST adjacent to YAs. Figure 3a shows the side and top views of YAs and the closely adjacent GST layer (i.e., interfacial layer). Clearly, after the melt-quenching process, the Ge, Sb, and Te atoms in this interfacial layer spontaneously form a crystalline-like arrangement, well matching the YAs template, in the amorphous structure. All Ge atoms occupy the cation sites and form bonds with As atoms below, with Sb and Te exhibiting only low densities of antisite defects (0.003 $Å^{-2}$ for Sb and 0.006 $Å^{-2}$ for Te atoms in our model). Moreover, four vacancies (accounting for 11.1% of all sites) in this interface GST layer represent a key feature of the rock-salt GST [52, 55]. The top GST interfacial layer (formed because of the periodic boundary) is shown in Figure S3. Moreover, the interfacial structure in the high-temperature melting process is shown in Figure S4. The GST atoms close to the YAs are disordered at 1500 K. At 1100 K, this layer becomes relatively ordered, especially since many Te atoms already occupy the correct lattice sites and form bonds with the underlying Y atoms. During the subsequent quenching process, this layer undergoes further structural refinement, achieving the cubic-like layer in the amorphous structure at room temperature (300 K). Figure 3b shows the time evolution of the ratios of Ge, Sb, and Te atoms and vacancies in these interfacial layers throughout the 120 ps crystallization process in the YAs-GST system. Note that the number of vacancies is calculated by subtracting the number of Ge, Sb, and Te atoms from the total lattice sites. The atomic proportions remain generally stable and in close agreement with the stoichiometry of $Ge_2Sb_2Te_5$. These results suggest that YAs can stabilize a rock-salt-like GST atomic layer after melt-quenching and provide an efficient template for later crystallization, avoiding the traditional stochastic nucleation period in GST [8, 27].

In fact, the YAs not only modulates the structure of the interfacial GST layer but also influences the structure of the adjacent GST regions. Figure 3c,d illustrates the Peierls distortion [56] of the amorphous region in the two structures, measured by the angular-limited three-body correlation (ALTBC). Due to the size limitations of the (MD) model, the GST in the coherent interface structure represents the region near the interface in actual devices. The intensity maps of ALTBC show the bond-length distribution of the near-linear bond pairs with bonding angles close to 180°. In the amorphous bulk GST, significant Peierls distortion is observed, with two distinct peaks at $r_1 = 3.2$ Å, $r_2 = 2.9$ Å, as well as the symmetric position ($r_1 = 2.9$ Å, $r_2 = 3.2$ Å). In contrast, the amorphous GST in the YAs coherent interface structure only shows one major peak at $r_1 = r_2 = 3.05$ Å, closer to the case of the rock-salt crystalline GST. Clearly, the nondistorted rock-salt YAs, shown in the inset in Figure 3c, suppressed the Peierls distortion of the adjacent amorphous GST. Figure 3e compares the coordination number of Ge atoms in the two structures. Previous studies have highlighted that the change of the position and coordination environment of Ge atoms is crucial in the amorphous-to-crystalline phase transition in GST [57, 58]. In the bulk structure, there are large numbers of 4-, 5-, and 6-coordinated Ge atoms, suggesting that Ge mainly occupies tetrahedral, octahedral, and defect octahedral positions. In contrast, in YAs-GST, the number of 4-coordinated atoms decreases, while 5-coordinated Ge atoms dominate, indicating that the sp^3 covalent bonding is weakened in amorphous GST and the *p*-orbital bonding network is strengthened, which is the key feature in crystalline phase-change memory [59, 60]. In Figure 3f, the bond angle distributions in the two models remain similar, implying that YAs has little influence on the bond angle

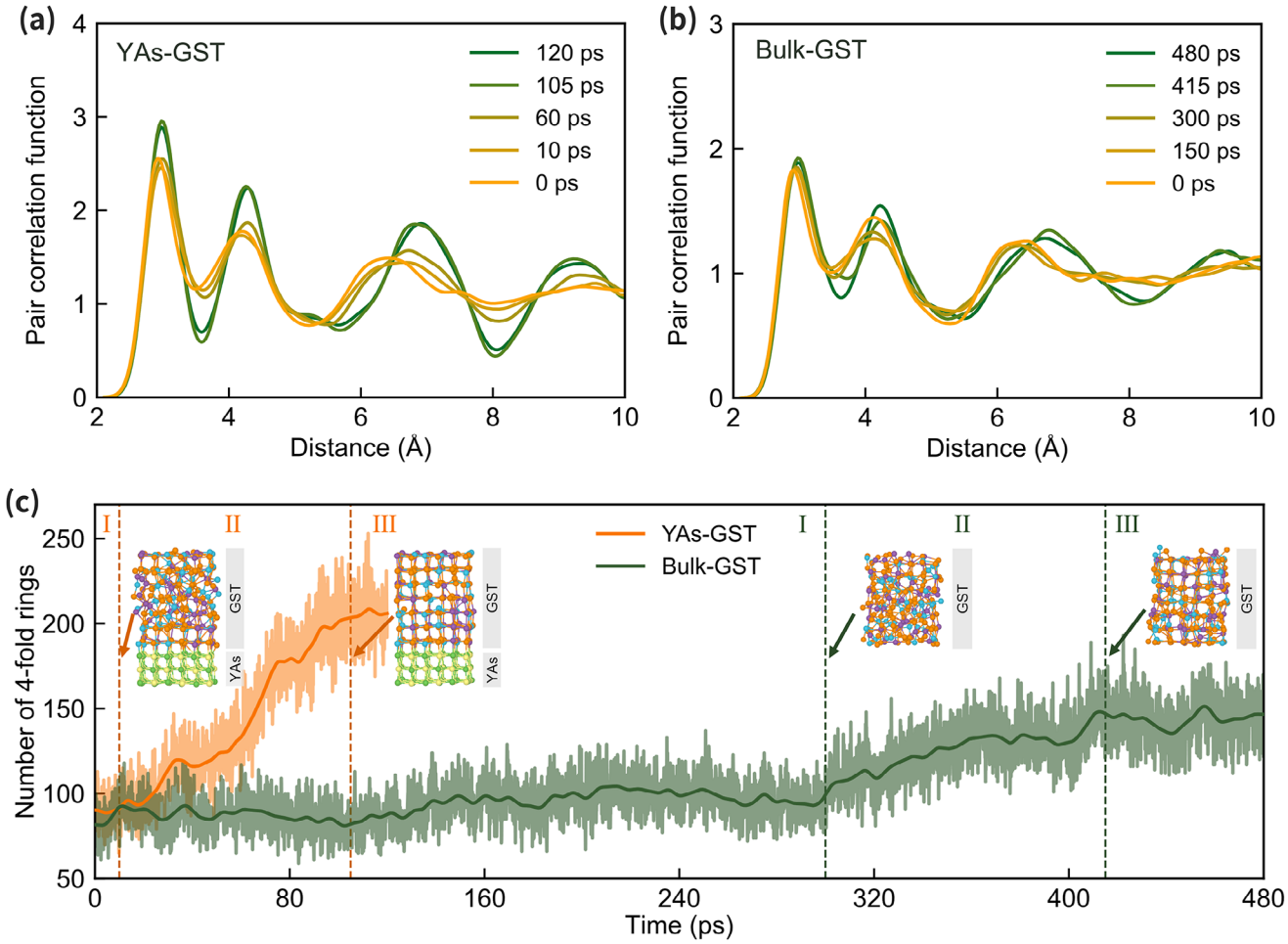

FIGURE 2 | Time evolution of pair correlation function (PCF) and fourfold rings in the crystallization process at 600 K. (a) PCF of GST in the interface structure. (b) PCF of GST in the bulk structure. (c) Fourfold rings of the GST in the interface structure and bulk structure. Internal snapshots present the atomic structures at different crystallization stages. Stages I, II, and III refer to the incubation period, crystallization development period, and slow-evolution period, respectively.

distribution of the amorphous GST. Yet, at around 110°, a slight decrease can be observed in the YAs-GST structure, once again indicating that fewer Ge atoms occupy tetrahedron centers.

We note that the key innovation of our strategy is the direct growth of the PCM material from the coherent interface formed between GST and another heterogeneous crystalline material, which has differences from the mechanisms of previous doping methods [8, 61]. For example, the Sc-doping method (i.e., Sc doping in Sb_2Te_3) relies on the stronger Sc—Te bonds to stabilize fourfold rings and cubes to accelerate the nucleation process [8], while Y-doping method (i.e., *Y* doping in Sb_2Te_3) employs *Y* atoms to twist the lattice, retard crystallization, refine the crystal grains, and consequently improve the crystallization speed [61].

So far, we have theoretically confirmed that the introduced coherent interfaces are able to greatly promote the crystallization of PCM materials. We believe that the acceleration mechanism (revealed through the example of YAs-$Ge_2Sb_2Te_5$ here) should also be applicable in other coherent interfaces formed between suitable crystalline materials and PCM materials, and help to achieve higher SET speed in the devices for the SCM applications. Following the above DFT-based molecular dynamics and structural analyses, we also carried out preliminary experimental studies of our coherent interface strategy. These results are presented in detail in Note S1 and Figure S5. Our YAs-GST device shows a faster SET speed and a lower SET voltage than those of the pure GST device.

2.3 | High-Throughput Screening of Coherent Interfaces

Although the role of coherent interfaces in PCM devices is illustrated using YAs, the mechanism should be general for other similar materials. In this session, we perform high-throughput screening to identify as many candidate materials as possible for constructing coherent interfaces with GST from the Materials Project database (containing over 150 000 structures) [62]. Our screening strategy consists of four criteria listed as follows.

- *Rock-salt binary compounds*: This criterion ensures that the anion and cation sublattices of the candidate material are compatible with rock-salt GST, which is a basic requirement for coherent interfaces.

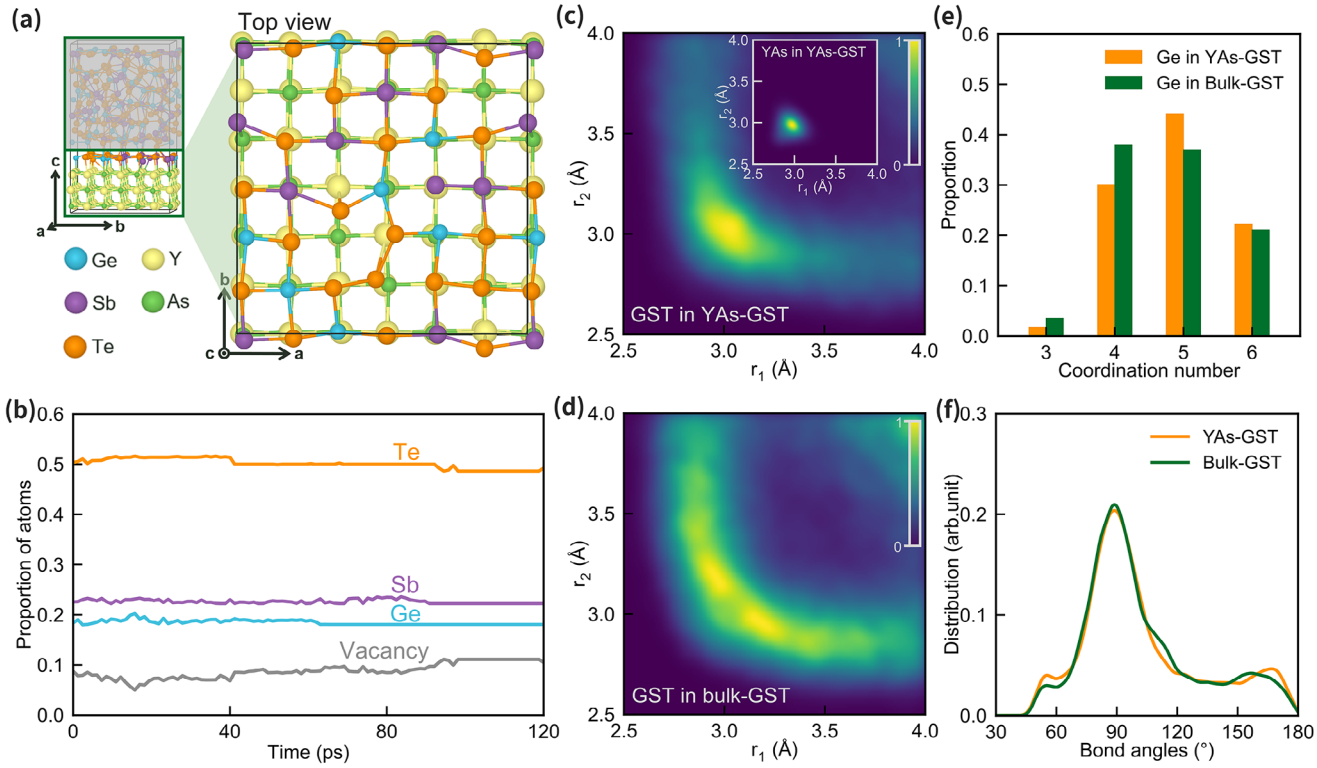

FIGURE 3 | Analysis and comparison of the amorphous GST in coherent interface structure (YAs-GST) and bulk structure (bulk-GST). (a,b) Side/Top view of the GST interfacial layer closely next to YAs and the proportions of Ge, Sb, Te, and vacancies in the layers over the 120 ps crystallization process. (c, d) The angular-limited three-body correlation (indicating Peierls distortion) of YAs (shown in the inset)/GST in YAs-GST, and GST in bulk-GST. (e) The coordination number of Ge in YAs-GST and bulk-GST. (f) Distribution of bond angles in YAs-GST and bulk-GST.

- *Stable structure*: We use the energy above hull (E_{hull}) from the Materials Project database to evaluate the thermodynamic stability of materials, requiring $E_{hull} < 0.1$ eV/atom to ensure that the rock-salt structure is stable or metastable and thus feasible for practical phase-change memory devices.
- *Lattice matching*: The lattice constant of the candidate should differ from GST by less than 5% to minimize dislocations and achieve high-quality coherent interfaces.
- *High melting point*: The melting point of the candidate material should be much higher than that of GST to withstand the high temperature in the RESET operation. We use cohesive energy as an indicator of melting point [63], and necessitate the cohesive energy > 4 eV/atom (compared to 2.85 eV/atom for GST). The complete screening process, criteria, and the number of materials remaining after each step are summarized in Figure 4a. Ultimately, we identified 71 candidates with detailed information provided in Table 1.

Under appropriate fabrication processes, these 71 candidates have the potential to introduce coherent interfaces in PCM materials and thus improve the SET speed. However, as we may face challenges in trying to construct coherent interfaces due to lack of sputtering target for some candidates and the resulting formation of complicated secondary phases by a single target sputtering, just like the Y—As—Ge—Sb—Te target used in the experiment (see Note S1 and Figure S5), we further proposed an extra screening process to identify candidates that may spontaneously aggregate in the phase-change materials to form crystals and coherent interfaces after single-target sputtering, as shown in Figure 4b. For the 71 materials screened above, we examined each of them, comparing its cohesive energy with those of all the possible binary compounds formed between its constituent elements and Ge, Sb, or Te. In detail, a candidate compound AB would be thermodynamically favorable for spontaneous aggregation if its cohesive energy is over 0.5 eV/atom higher than all binary compounds that can form between A/B and Ge/Sb/Te. Based on this analysis, we further identified 14 easily formed candidates for single-target sputtering under limited fabrication conditions, shown in Table S1.

Figure 4c shows the distribution of 248 stable binary rock-salt structures that pass the first two screening criteria in Figure 4a in terms of lattice constants and cohesive energy. Each point in the picture represents a structure, and the orange region refers to the range that meets all four criteria. It can be observed that the area with a lattice constant between 4.8 and 6.8 Å and cohesive energy exceeding 4 eV forms a relatively dense cluster. The final candidates fall entirely inside this area, encompassing 71 structures. The 14 structures further screened in Figure 4b are shown as orange dots with blue rings. Figure 4d illustrates the element distribution of the 71 candidates. The number below the element symbol represents its frequency among the candidates. Two obvious groups emerge: anions are concentrated in six elements of Se, As, Sb, Te, Bi, and P, with small amounts distributed in Ge and S. The cation elements are widely found in Group IIIB, relatively evenly distributed across Sc, Y, lanthanides, and actinides. In particular, among the 15 lanthanide elements,

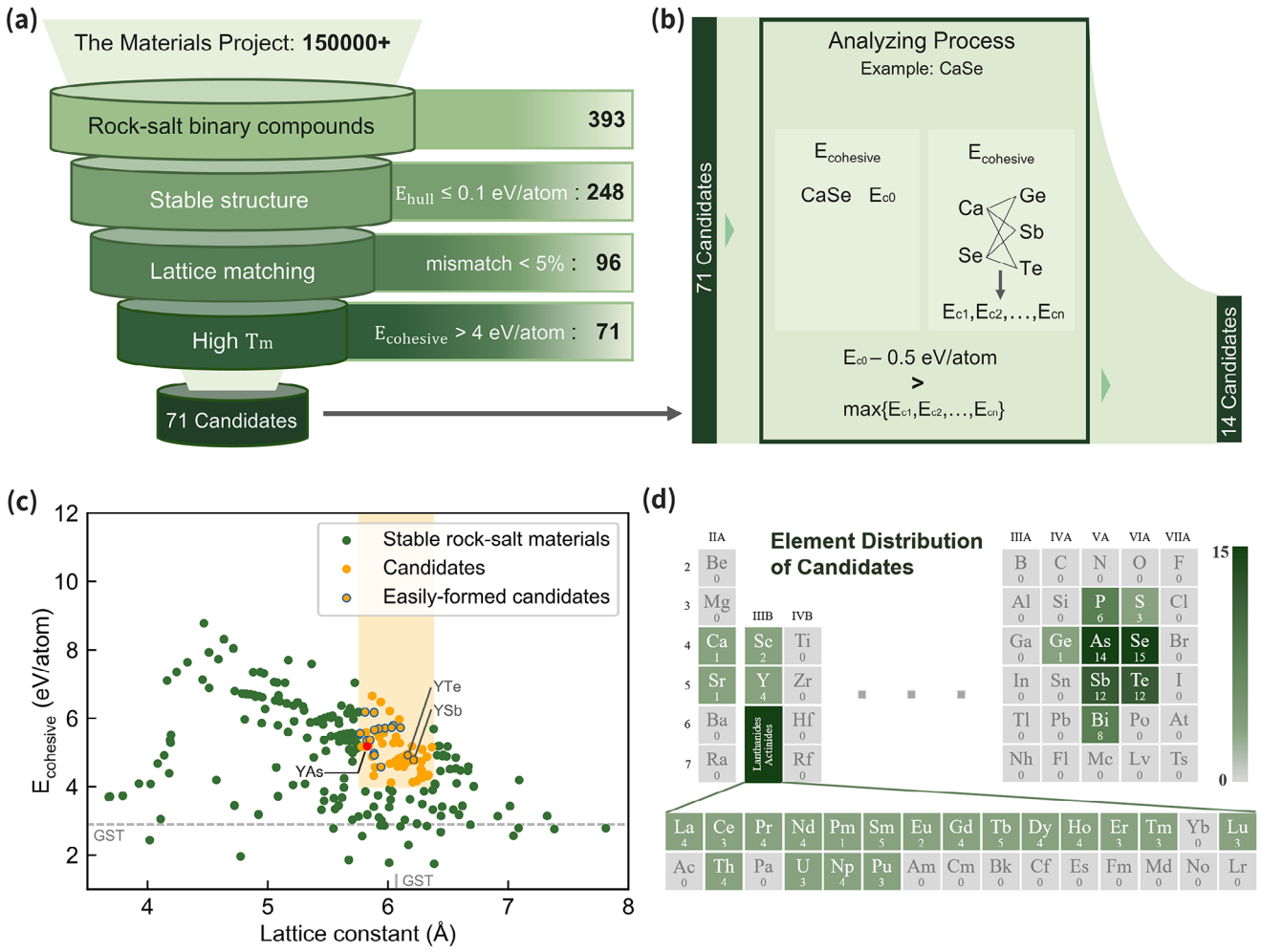

FIGURE 4 | High-throughput screening strategy and potential candidates. (a) High-throughput screening strategy. Four tiers of screening criteria, including rock-salt structure, thermodynamic stability, lattice matching, and melting temperature, are employed on the Materials Project database. The screening starts from 150 000+ material structures, and the number of selected structures at each tier is provided. Finally, 71 candidates are selected. (b) An extra analyzing process for identifying 14 easily formed candidates that may be suitable for single-target sputtering from all the 71 candidates. (c) Distribution of lattice constants and cohesive energies among 248 stable binary rock-salt structures that pass the first two screening criteria in (a). The orange area contains the final 71 candidates. Orange dots with blue rings refer to the 14 easily formed candidates identified in (b). The positions of YAs, YTe, and YSb are also highlighted. (d) Element distribution of the 71 candidates. The number below each element symbol represents the frequency.

only Yb is absent. We chose four representative materials from the 71 candidates and calculated their band structures with HSE hybrid functional to gain accurate results, with results shown in Figure S6.

Our work focuses on $Ge_2Sb_2Te_5$, which is the popular nucleation-driven PCM material. In addition, accelerating crystallization of growth-dominated PCM materials could also benefit from our coherent-interface strategy and corresponding screening. Here, we take GeTe as an example for explanation. Generally, its amorphous phase would first crystallize into the rock-salt cubic phase at high temperatures [64]. Although the nucleation rate of GeTe is slow, the rock-salt-lattice-matching coherent interface can directly offer an effective template for the fast growth of the cubic phase from the interface. The screening of compounds to form a coherent interface with rock-salt GST can also be applied to the rock-salt GeTe due to their close lattice parameters. Among all the 71 candidates identified, the largest lattice mismatch with cubic GeTe is only about 6%.

We also understand that the crystallization speed of the amorphous phase and data retention are often in competition, and thus further measured the data retention ability of the YAs-GST film. In Figure S7, the 10-year data-retention temperature of YAs-incorporated GST is evaluated to be 73°C, which is modestly smaller than that of pure GST (~85°C) [65]. This modest decrease is consistent with the physical intuition.

In our current work, we used YAs as an example to demonstrate our strategy. In principle, the crystallization of GST based on a coherent interface should occur through direct growth from the interface. Therefore, the enlarged coherent interfaces withGST would more effectively facilitate crystallization. We note that although YAs has been known since 1960 [48], it has received limited attention, and the target of YAs is currently not readily available. With access to the YAs sputtering target in the future, we would be able to perform co-sputtering of YAs and GST, or optimize the deposition sequence between the two materials to form well-defined YAs layered structures and consequently form

TABLE 1 | 71 candidate materials to form coherent interfaces with rock-salt GST and detailed information. In the table, mp-id represents the material ID in the Materials Project database. E_{hull} represents the energy above the hull. E_c represents the cohesive energy. Lattice constants are also shown.

mp-id	Formula	E_{hull} (eV/atom)	Lattice constant (Å)	E_c (eV/atom)
mp-1415	CaSe	0	5.942	4.578
mp-2748	CeAs	0	6.087	5.292
mp-2154	CeP	0	5.926	5.638
mp-2563	CeSe	0	6.043	5.789
mp-2627	DyAs	0	5.808	5.194
mp-22907	DyBi	0	6.311	4.312
mp-1007	DySb	0	6.192	4.76
mp-2159	DyTe	0	6.142	4.909
mp-23245	ErBi	0	6.262	4.228
mp-2191	ErSb	0	6.142	4.684
mp-1280	ErTe	0	6.085	4.803
mp-20587	EuS	0	5.884	4.976
mp-21009	EuSe	0	6.13	4.588
mp-510374	GdAs	0	5.89	4.922
mp-510403	GdSb	0	6.273	4.52
mp-510404	GdSe	0	5.825	5.349
mp-574283	GdTe	0.065	6.227	4.767
mp-295	HoAs	0	5.78	5.171
mp-22866	HoBi	0	6.287	4.274
mp-2050	HoSb	0	6.163	4.726
mp-919	HoTe	0	6.113	4.86
mp-708	LaAs	0	6.2	5.182
mp-2384	LaP	0	6.068	5.462
mp-2350	LaS	0	5.885	6.168
mp-1161	LaSe	0	6.104	5.724
mp-568059	LuBi	0	6.205	4.132
mp-516	LuSb	0	6.08	4.598
mp-1254	LuTe	0.06	6.015	4.67
mp-2602	NdAs	0	6.046	5.274
mp-2823	NdP	0	5.91	5.578
mp-1453	NdSe	0	5.975	5.713
mp-570	NdTe	0	6.366	5.158
mp-2186	NpAs	0	5.87	4.885
mp-20969	NpSb	0	6.279	4.38
mp-627	NpSe	0	5.85	5.366
mp-807	NpTe	0.044	6.28	4.738
mp-1232234	PmSe	0	5.922	5.699
mp-10622	PrAs	0	6.098	5.272
mp-601	PrP	0	5.964	5.566
mp-2495	PrS	0	5.809	6.183
mp-1674	PrSe	0	6.029	5.729
mp-2548	PuAs	0	5.881	4.324

(Continues)

TABLE 1 | (Continued)

mp-id	Formula	E_{hull} (eV/atom)	Lattice constant (Å)	E_c (eV/atom)
mp-2288	PuSe	0	5.886	4.921
mp-1556	PuTe	0	6.299	4.343
mp-570632	ScBi	0	6.026	4.119
mp-549	ScSb	0	5.893	4.57
mp-1738	SmAs	0	5.953	5.26
mp-710	SmP	0	5.819	5.582
mp-2281	SmSb	0	6.326	4.879
mp-1447	SmSe	0	5.888	5.662
mp-342	SmTe	0	6.284	5.089
mp-2758	SrSe	0	6.281	4.472
mp-2640	TbAs	0	5.841	5.213
mp-22921	TbBi	0	6.336	4.347
mp-2724	TbSb	0	6.219	4.79
mp-1561	TbSe	0	5.769	5.556
mp-1176	TbTe	0.014	6.167	4.955
mp-1753	ThAs	0	6.015	6.215
mp-1093	ThGe	0	6.094	5.97
mp-931	ThP	0	5.869	6.647
mp-2183	ThSe	0	5.941	6.48
mp-23234	TmBi	0	6.242	4.165
mp-2520	TmSb	0	6.121	4.625
mp-237	TmTe	0.038	6.057	4.727
mp-2104	UAs	0	5.927	5.454
mp-519	USb	0.071	6.201	4.866
mp-2143	USe	0	5.914	5.647
mp-933	YAs	0	5.827	5.182
mp-23241	YBi	0	6.332	4.318
mp-215	YSb	0	6.213	4.76
mp-1708	YTe	0.027	6.162	4.908

a desired YAs/GST interface for more effective crystallization. We also verified our strategy with ScSb, another candidate obtained from the high-throughput screening, by extra AIMD simulations (Figure S8). It is shown that ScSb also successfully facilitates the fast recrystallization of GST via the coherent interface. Therefore, the strategy of a coherent interface is robust.

3 | Conclusion

In summary, the research here proposes a new strategy to realize ultrafast nonstochastic crystallization by embedding coherent interfaces into the PCM materials for high-speed PCM device applications. Taking YAs, a material that has largely been overlooked before, as an example, we construct a coherent interface with GST, and demonstrate a remarkably fast and nonstochastic crystallization behavior in PCM materials by first-principles molecular dynamics. The YAs exhibits excellent high-temperature stability and forms strong covalent bonds with GST materials. As a result, a rock-salt-like atomic interfacial layer (next to YAs) is retained in the amorphous GST after the melt-quenching process. The interfacial layer can act as an ideal medium, not only preserving the rock-salt-like structural features from YAs, but also ensuring electronic and chemical compatibility with the inner GST. These features enable amorphous GST to switch back to the crystalline state at the appropriate temperature without a prolonged stochastic nucleation process. Device experiments further demonstrate that the SET speed of YAs-incorporated GST significantly increases even under a lower voltage, compared with pure GST (see Note S1 and Figure S5). Finally, employing four-tier high-throughput screening, including rock-salt structure, thermodynamic stability, lattice matching, and melting point, we further identified 71 potential candidates suitable for constructing coherent interfaces with GST, displaying its broad applicability. With the validated effectiveness of our strategy, continued close collaboration with industry partners

remains essential to achieve overall performance improvements in PCM devices by embedding coherent interfaces in the future. The present work establishes a promising new strategy to achieve high-speed PCM via atomic-scale interface design for future storage-class-memory implementation.

4 | Experimental Section

4.1 | First-Principles Calculations and Molecular Dynamics

The first-principles calculations employed density functional theory (DFT) implemented in the Vienna Ab initio Simulation Package (VASP) [66] code. The coherent interface structure containing 334 atoms (including 54 *Y*, 54 As, 50 Ge, 50 Sb, and 126 Te) was constructed, where the cation and anion sublattices in YAs and GST perfectly matched at the interface. A bulk GST structure with 50 Ge, 50 Sb, and 126 Te atoms was also prepared for comparison. The electronic exchange-correlation interaction was described with the Perdew-Burke-Ernzerhof (PBE) functional [67] in the calculations of the interface structure and bulk GST structure. The DFT-D3 method was used to include the vdW interactions in the calculations [68]. The crystal orbital Hamilton population (COHP), integrated COHP (ICOHP), and integrated crystal orbital bond index (ICOBI) were implemented with the LOBSTER program [51, 69]. In the first-principles molecular dynamics (MD) simulations, we employed the NVT canonical ensemble, where the Nosé-thermostat is used to control the temperature [70]. The time step of 3 fs, energy cutoff of 350 eV, and a single *k*-point were used for this structure in the MD process. The amorphous interface structure was prepared using the melt-quenching method. The structure was melted at 1500 K for 9 ps and equilibrated at 1100 K for 15 ps. Considering that the stability of YAs in this structure had been confirmed in 1500 K MD, the positions of the Y and As atoms in the middle layer of YAs are fixed, with the top and bottom YAs layers unfixed, in the high-temperature process to avoid the center-of-mass drift. Finally, it was quenched to 300 K and maintained for another 15 ps, with all atoms unfixed. For comparison, a bulk GST model was also obtained using the same melt-quenching method, except for the absence of the interface. All the structures were visualized through VESTA [71]. In the calculations of the band structures of YAs, CaSe, ScSb, and LaAs, the energy cutoffs were set to 1.5 times the maximum ENMAX (recommended energy cutoff by VASP), the effect of spin polarization was included, and the $9 \times 9 \times 9$ Monkhorst–Pack [72] *k*-point grid was used.

4.2 | PCM Device Fabrication and Electrical Measurement

A Pt bottom electrode with a thickness of 100 nm was sputter-deposited onto the SiO_2/Si substrate. Subsequently, a SiO_2 insulator layer with a thickness of 100 nm was deposited by plasma-enhanced chemical vapor deposition (PECVD) to isolate different cells. Electron beam lithography (EBL) was employed to create through-hole patterns measuring 250 nm in diameter and also create bottom electrode square patterns of 100×100 µm. Inductively coupled plasma (ICP) etching was then used to create the through-holes and bottom electrodes. The photolithography step was carried out to define 150×150 µm square patterns for the top electrodes above the center of the through-hole array. Afterward, using a $Y_{0.3}As_{0.3}Ge_2Sb_2Te_5$ sputtering target, a 100 nm-thick material was sputter-deposited as the phase-change layer, and a Pt film of the same thickness was deposited as the top electrode. Through the lift-off process, the final device was achieved. As the control group, GST devices were fabricated using the same process, except that $Ge_2Sb_2Te_5$ was deposited as the phase-change material. The electrical properties of the fabricated devices were characterized by Keysight B1500A semiconductor device parameter analyzer, which could produce voltage pulses to SET the phase-change memory devices.

4.3 | High-Throughput Screening

The initial data that support the high-throughput screening section in this paper, including E_{hull}, lattice constant, and E_c, were collected through the open Materials Application Programming Interface (API) [73] from the Materials Project database (Database v2025.02) [62].

Acknowledgements

This work was supported by the National Key Research and Development Program of China (Grant No. 2024YFA1208701), the National Natural Science Foundation of China (Grant Nos. 12274172 and 12274180), the Science and Technology Development Plan Project of Changchun, China (Grant No. 2024GZZ07), and the Fundamental Research Funds for the Central Universities. The High-Performance Computing Center (HPCC) at Jilin University for computational resources is also acknowledged. We sincerely thank Prof. Feng Ding, Prof. Yan Cheng, and Mr. Hongda Jiang for helpful discussions and support.

Funding

The National Key Research and Development Program of China (Grant No. 2024YFA1208701), the National Natural Science Foundation of China (Grant Nos. 12274172 and 12274180), the Science and Technology Development Plan Project of Changchun, China (Grant No. 2024GZZ07), and the Fundamental Research Funds for the Central Universities.

Conflicts of Interest

The authors declare no conflicts of interest.

Data Availability Statement

The data that support the findings of this study are available from the corresponding author upon reasonable request.

References

1. W. Zhang, R. Mazzarello, M. Wuttig, and E. Ma, "Designing Crystallization in Phase-Change Materials for Universal Memory and Neuro-Inspired Computing," *Nature Reviews Materials* 4 (2019): 150–168, https://doi.org/10.1038/s41578-018-0076-x.

2. K. Ishimaru, "Future of Non-Volatile Memory-From Storage to Computing, " paper presented at the Conference 2019 IEEE International Electron Devices Meeting (IEDM), San Francisco, CA, USA, December 7–11, 2019.

3. S. W. Fong, C. M. Neumann, and H. S. P. Wong, "Phase-Change Memory—Towards a Storage-Class Memory," *IEEE Transactions on Electron Devices* 64 (2017): 4374–4385, https://doi.org/10.1109/TED.2017.2746342.

4. S.-O. Park, S. Hong, S.-J. Sung, et al., "Phase-Change Memory via a Phase-Changeable Self-Confined Nano-Filament," *Nature* 628 (2024): 293–298, https://doi.org/10.1038/s41586-024-07230-5.

5. H.-S. P. Wong, S. Raoux, S. Kim, et al., "Phase Change Memory," *Proceedings of the IEEE* 98 (2010): 2201, https://doi.org/10.1109/JPROC.2010.2070050.

6. Y. Zhou, W. Zhang, E. Ma, and V. L. Deringer, "Device-Scale Atomistic Modelling of Phase-Change Memory Materials," *Nature Electronics* 6 (2023): 746–754, https://doi.org/10.1038/s41928-023-01030-x.

7. D. Lencer, M. Salinga, and M. Wuttig, "Design Rules for Phase-Change Materials in Data Storage Applications," *Advanced Materials* 23 (2011): 2030–2058, https://doi.org/10.1002/adma.201004255.

8. F. Rao, K. Ding, Y. Zhou, et al., "Reducing the Stochasticity of Crystal Nucleation to Enable Subnanosecond Memory Writing," *Science* 358 (2017): 1423–1427, https://doi.org/10.1126/science.aao3212.

9. K. Aryana, J. T. Gaskins, J. Nag, et al., "Interface Controlled Thermal Resistances of Ultra-Thin Chalcogenide-Based Phase Change Memory Devices," *Nature Communications* 12 (2021): 774, https://doi.org/10.1038/s41467-020-20661-8.

10. J. Shen, S. Jia, N. Shi, et al., "Elemental Electrical Switch Enabling Phase Segregation–Free Operation," *Science* 374 (2021): 1390–1394, https://doi.org/10.1126/science.abi6332.

11. X.-B. Li, N.-K. Chen, X.-P. Wang, and H.-B. Sun, "Phase-Change Superlattice Materials Toward Low Power Consumption and High Density Data Storage: Microscopic Picture, Working Principles, and Optimization," *Advanced Functional Materials* 28 (2018): 1803380, https://doi.org/10.1002/adfm.201803380.

12. Z. Zhang, Z. Wang, T. Shi, et al., "Memory Materials and Devices: From Concept to Application," *InfoMat* 2 (2020): 261–290, https://doi.org/10.1002/inf2.12077.

13. J. Huang, B. Chen, G. Sha, et al., "Nanoscale Chemical Heterogeneity Ensures Unprecedently Low Resistance Drift in Cache-Type Phase-Change Memory Materials," *Nano Letters* 23 (2023): 2362–2369, https://doi.org/10.1021/acs.nanolett.3c00262.

14. Y. Zeng, H. Li, Y. Zhu, et al., "Introducing Spontaneously Phase-Separated Heterogeneous Interfaces Enables Low Power Consumption and High Reliability for Phase Change Memory," *Advanced Electronic Materials* 8 (2022): 2200437, https://doi.org/10.1002/aelm.202200437.

15. W. Kim, M. BrightSky, T. Masuda, et al., "ALD-Based Confined PCM With a Metallic Liner Toward Unlimited Endurance, " paper presented at Conference on 2016 IEEE International Electron Devices Meeting (IEDM), San Francisco, CA, USA, December 3–7, 2016.

16. M.-H. Shao, R.-T. Zhao, H. Liu, et al., "Challenges and Recent Advances in HfO_2-Based Ferroelectric Films for Non-Volatile Memory Applications," *Chip* 3 (2024): 100101, https://doi.org/10.1016/j.chip.2024.100101.

17. Y. Sun, J. Li, S. Li, et al., "Advanced Synaptic Devices and Their Applications in Biomimetic Sensory Neural System," *Chip* 2 (2023): 100031, https://doi.org/10.1016/j.chip.2022.100031.

18. Z. Fang, R. Chen, J. Zheng, et al., "Ultra-Low-Energy Programmable Non-Volatile Silicon Photonics Based on Phase-Change Materials With Graphene Heaters," *Nature Nanotechnology* 17 (2022): 842–848, https://doi.org/10.1038/s41565-022-01153-w.

19. Wikipedia Contributors, "3D Xpoint," https://en.wikipedia.org/w/index.php?title=3D_XPoint&oldid=1333246558.

20. I. B. Peng, M. B. Gokhale, and E. W. Green, "System Evaluation of the Intel Optane Byte-Addressable Nvm," in *Proceedings of the International Symposium on Memory Systems*, ed. B. Jacob (ACM Digital Library, 2019), 304–315.

21. Intel Corporation, "Intel and Micron Produce Breakthrough Memory Technology," published July 28, 2015, https://www.intc.com/news-events/press-releases/detail/324/intel-and-micron-produce-breakthrough-memory-technology.

22. K.-H. Kim, I. Karpov, R. H. Olsson, and D. Jariwala, "Wurtzite and Fluorite Ferroelectric Materials for Electronic Memory," *Nature Nanotechnology* 18 (2023): 422–441, https://doi.org/10.1038/s41565-023-01361-y.

23. M. Salinga, E. Carria, A. Kaldenbach, et al., "Measurement of Crystal Growth Velocity in a Melt-Quenched Phase-Change Material," *Nature Communications* 4 (2013): 2371, https://doi.org/10.1038/ncomms3371.

24. M. Xu, X. Mai, J. Lin, et al., "Recent Advances on Neuromorphic Devices Based on Chalcogenide Phase-Change Materials," *Advanced Functional Materials* 30 (2020): 2003419, https://doi.org/10.1002/adfm.202003419.

25. F. Ding, B. Peng, X. Li, et al., "A Review of Compact Modeling for Phase Change Memory," *Journal of Semiconductors* 43 (2022): 023101, https://doi.org/10.1088/1674-4926/43/2/023101.

26. Y. Chen, D. Campi, M. Bernasconi, and R. Mazzarello, "Atomistic Study of the Configurational Entropy and the Fragility of Supercooled Liquid GeTe," *Advanced Functional Materials* 34 (2024): 2314264, https://doi.org/10.1002/adfm.202314264.

27. M. Wuttig and N. Yamada, "Phase-Change Materials for Rewriteable Data Storage," *Nature Materials* 6 (2007): 824–832, https://doi.org/10.1038/nmat2009.

28. D. Loke, T. H. Lee, W. J. Wang, et al., "Breaking the Speed Limits of Phase-Change Memory," *Science* 336 (2012): 1566–1569, https://doi.org/10.1126/science.1221561.

29. B. Prasai, G. Chen, and D. A. Drabold, "Direct Ab-Initio Molecular Dynamic Study of Ultrafast Phase Change in Ag-Alloyed $Ge_2Sb_2Te_5$," *Applied Physics Letters* 102 (2013): 041907, https://doi.org/10.1063/1.4789877.

30. S. Kohara, K. Kato, S. Kimura, et al., "Structural Basis for the Fast Phase Change of $Ge_2Sb_2Te_5$: Ring Statistics Analogy Between the Crystal and Amorphous States," *Applied Physics Letters* 89 (2006): 201910, https://doi.org/10.1063/1.2387870.

31. Y. Wang, Y. Zheng, G. Liu, et al., "Scandium Doped $Ge_2Sb_2Te_5$ for High-Speed and Low-Power-Consumption Phase Change Memory," *Applied Physics Letters* 112 (2018): 133104, https://doi.org/10.1063/1.5012872.

32. M. Zhu, M. Xia, F. Rao, et al., "One Order of Magnitude Faster Phase Change at Reduced Power in Ti-Sb-Te," *Nature Communications* 5 (2014): 4086, https://doi.org/10.1038/ncomms5086.

33. L. Cao, X. Ji, W. Zhu, et al., "Advantage of Ti-Doped $Ge_2Sb_2Te_5$ Material for Phase Change Memory Applications," *ECS Solid State Letters* 4 (2015): P102, https://doi.org/10.1149/2.0081512ssl.

34. R. Wang, Z. Song, W. Song, et al., "Phase-Change Memory Based on Matched Ge-Te , Sb-Te, and In-Te Octahedrons: Improved Electrical Performances and Robust Thermal Stability," *InfoMat* 3 (2021): 1008–1015, https://doi.org/10.1002/inf2.12233.

35. Y. Zeng, J. Jin, R. Gu, et al., "A Fast and High Endurance Phase Change Memory Based on In-Doped Sb_2Te_3," *ACS Applied Nano Materials* 7 (2024): 13983–13990, https://doi.org/10.1021/acsanm.4c00809.

36. R. E. Simpson, P. Fons, A. V. Kolobov, et al., "Interfacial Phase-Change Memory," *Nature Nanotechnology* 6 (2011): 501–505, https://doi.org/10.1038/nnano.2011.96.

37. B.-Q. Wang, T.-Y. Zhao, H.-R. Ding, et al., "Partial Melting Nature of Phase-Change Memory Ge-Sb-Te Superlattice Uncovered by Large-Scale Machine Learning Interatomic Potential Molecular Dynamics," *Acta Materialia* 276 (2024): 120123, https://doi.org/10.1016/j.actamat.2024.120123.

38. C. Yoo, J. W. Jeon, S. Yoon, et al., "Atomic Layer Deposition of Sb_2Te_3/GeTe Superlattice Film and Its Melt-Quenching-Free Phase-

Transition Mechanism for Phase-Change Memory," *Advanced Materials* 34, (2022): 2207143, https://doi.org/10.1002/adma.202207143.

39. K. L. Okabe, A. Sood, E. Yalon, et al., "Understanding the Switching Mechanism of Interfacial Phase Change Memory," *Journal of Applied Physics* 125 (2019): 184501, https://doi.org/10.1063/1.5093907.

40. A. I. Khan, A. Daus, R. Islam, et al., "Ultralow–Switching Current Density Multilevel Phase-Change Memory on a Flexible Substrate," *Science* 373 (2021): 1243–1247, https://doi.org/10.1126/science.abj1261.

41. K. Ding, J. Wang, Y. Zhou, et al., "Phase-Change Heterostructure Enables Ultralow Noise and Drift for Memory Operation," *Science* 366 (2019): 210–215, https://doi.org/10.1126/science.aay0291.

42. S. W. Park, H. J. Lee, K. A. Nirmal, et al., "Phase-Change Heterostructure With $HfTe_2$ Confinement Sublayers for Enhanced Thermal Efficiency and Low-Power Operation Through Joule Heating Localization," *Journal of Materials Science & Technology* 204 (2025): 104–114, https://doi.org/10.1016/j.jmst.2024.02.072.

43. J. Feng, A. Lotnyk, H. Bryja, et al., "Stickier″-Surface Sb_2Te_3 Templates Enable Fast Memory Switching of Phase Change Material $GeSb_2Te_4$ With Growth-Dominated Crystallization," *ACS Applied Materials & Interfaces* 12 (2020): 33397–33407, https://doi.org/10.1021/acsami.0c07973.

44. R. Zhao, K. Gao, R. Zhu, et al., "650 ps SET Speed in $Ge_2Sb_2Te_5$ Phase Change Memory Induced by TiO_2 Dielectric Crystal Plane," *InfoMat* 6 (2024): 12598, https://doi.org/10.1002/inf2.12598.

45. B. P. Uberuaga, P. P. Dholabhai, G. Pilania, and A. Chen, "Semicoherent Oxide Heterointerfaces: Structure, Properties, and Implications," *APL Materials* 7 (2019): 100904, https://doi.org/10.1063/1.5121027.

46. J. Zhang, G. Liu, W. Cui, et al., "Plastic Deformation in Silicon Nitride Ceramics via Bond Switching at Coherent Interfaces," *Science* 378 (2022): 371–376, https://doi.org/10.1126/science.abq7490.

47. Z. Li, Z. Zhang, X. Liu, et al., "Strength, Plasticity and Coercivity Tradeoff in Soft Magnetic High-Entropy Alloys by Multiple Coherent Interfaces," *Acta Materialia* 254 (2023): 118970, https://doi.org/10.1016/j.actamat.2023.118970.

48. L. Brixner, "Structure and Electrical Properties of Some New Rare Earth Arsenides, Antimonides and Tellurides," *Journal of Inorganic and Nuclear Chemistry* 15 (1960): 199–201, https://doi.org/10.1016/0022-1902(60)80038-3.

49. Q.-J. Hong, S. V. Ushakov, A. van de Walle, and A. Navrotsky, "Melting Temperature Prediction Using a Graph Neural Network Model: From Ancient Minerals to New Materials," *Proceedings of the National Academy of Sciences* 119 (2022): 2209630119, https://doi.org/10.1073/pnas.2209630119.

50. S. W. Ryu, J. H. Oh, J. H. Lee, et al., "Phase Transformation Behaviors of SiO_2 Doped $Ge_2Sb_2Te_5$ Films for Application in Phase Change Random Access Memory," *Applied Physics Letters* 92 (2008): 142110, https://doi.org/10.1063/1.2898719.

51. R. Dronskowski and P. E. Bloechl, "Crystal Orbital Hamilton Populations (COHP): Energy-Resolved Visualization of Chemical Bonding in Solids Based on Density-Functional Calculations," *Journal of Physical Chemistry* 97 (1993): 8617–8624, https://doi.org/10.1021/j100135a014.

52. M. Wuttig, D. Lüsebrink, D. Wamwangi, W. Wełnic, M. Gilleßen, and R. Dronskowski, "The Role of Vacancies and Local Distortions in the Design of New Phase-Change Materials," *Nature Materials* 6 (2007): 122–128, https://doi.org/10.1038/nmat1807.

53. P. C. Müller, C. Ertural, J. Hempelmann, and R. Dronskowski, "Crystal Orbital Bond Index: Covalent Bond Orders in Solids," *Journal of Physical Chemistry C* 125 (2021): 7959–7970, https://doi.org/10.1021/acs.jpcc.1c00718.

54. Y.-T. Liu, X.-B. Li, H. Zheng, et al., "High-Throughput Screening for Phase-Change Memory Materials," *Advanced Functional Materials* 31 (2021): 2009803, https://doi.org/10.1002/adfm.202009803.

55. J. Feng, M. Xu, X. Wang, et al., "Gold Fillings Unravel the Vacancy Role in the Phase Transition of GeTe," *Applied Physics Letters* 112 (2018): 071902, https://doi.org/10.1063/1.5006718.

56. N.-K. Chen, X.-B. Li, J. Bang, et al., "Directional Forces by Momentumless Excitation and Order-to-Order Transition in Peierls-Distorted Solids: The Case of GeTe," *Physical Review Letters* 120 (2018): 185701, https://doi.org/10.1103/PhysRevLett.120.185701.

57. S. Wintersteller, O. Yarema, D. Kumaar, et al., "Unravelling the Amorphous Structure and Crystallization Mechanism of GeTe Phase Change Memory Materials," *Nature Communications* 15 (2024): 1011, https://doi.org/10.1038/s41467-024-45327-7.

58. A. V. Kolobov, P. Fons, A. I. Frenkel, A. L. Ankudinov, J. Tominaga, and T. Uruga, "Understanding the Phase-Change Mechanism of Rewritable Optical media," *Nature Materials* 3 (2004): 703–708, https://doi.org/10.1038/nmat1215.

59. M. Wuttig, V. L. Deringer, X. Gonze, C. Bichara, and J. Y. Raty, "Incipient Metals: Functional Materials With a Unique Bonding Mechanism," *Advanced Materials* 30 (2018): 1803777, https://doi.org/10.1002/adma.201803777.

60. K. Shportko, S. Kremers, M. Woda, D. Lencer, J. Robertson, and M. Wuttig, "Resonant Bonding in Crystalline Phase-Change Materials," *Nature Materials* 7 (2008): 653–658, https://doi.org/10.1038/nmat2226.

61. B. Liu, W. Liu, Z. Li, et al., "Y-Doped Sb_2Te_3 Phase-Change Materials: Toward a Universal Memory," *ACS Applied Materials & Interfaces* 12 (2020): 20672–20679, https://doi.org/10.1021/acsami.0c03027.

62. A. Jain, S. P. Ong, G. Hautier, et al., "Commentary: The Materials Project: A Materials Genome Approach to Accelerating Materials Innovation," *APL Materials* 1 (2013): 011002, https://doi.org/10.1063/1.4812323.

63. V. Gharakhanyan, L. J. Wirth, J. A. G. Torres, et al., "Discovering Melting Temperature Prediction Models of Inorganic Solids by Combining Supervised and Unsupervised Learning," *Journal of Chemical Physics* 160 (2024): 204112, https://doi.org/10.1063/5.0207033.

64. G. C. Sosso, G. Miceli, S. Caravati, F. Giberti, J. Behler, and M. Bernasconi, "Fast Crystallization of the Phase Change Compound GeTe by Large-Scale Molecular Dynamics Simulations," *Journal of Physical Chemistry Letters* 4 (2013): 4241–4246, https://doi.org/10.1021/jz402268v.

65. F. M. Schenk, T. Zellweger, D. Kumaar, et al., "Phase-Change Memory From Molecular Tellurides," *ACS Nano* 18 (2024): 1063–1072, https://doi.org/10.1021/acsnano.3c10312.

66. G. Kresse and J. Furthmüller, "Efficient Iterative Schemes for Ab Initio Total-Energy Calculations Using a Plane-Wave Basis Set," *Physical Review B* 54 (1996): 11169, https://doi.org/10.1103/PhysRevB.54.11169.

67. J. P. Perdew, K. Burke, and M. Ernzerhof, "Generalized Gradient Approximation Made Simple," *Physical Review Letters* 77 (1996): 3865, https://doi.org/10.1103/PhysRevLett.77.3865.

68. S. Grimme, J. Antony, S. Ehrlich, and H. Krieg, "A Consistent and Accurate Ab Initio Parametrization of Density Functional Dispersion Correction (DFT-D) for the 94 Elements H-Pu," *Journal of Chemical Physics* 132 (2010): 154104, https://doi.org/10.1063/1.3382344.

69. R. Nelson, C. Ertural, J. George, V. L. Deringer, G. Hautier, and R. Dronskowski, "LOBSTER: Local Orbital Projections, Atomic Charges, and Chemical-Bonding Analysis From Projector-Augmented-Wave-Based Density-Functional Theory," *Journal of Computational Chemistry* 41 (2020): 1931–1940, https://doi.org/10.1002/jcc.26353.

70. N. Shuichi, "Constant Temperature Molecular Dynamics Methods," *Progress of Theoretical Physics Supplement* 103 (1991): 1–46, https://doi.org/10.1143/ptps.103.1.

71. K. Momma and F. Izumi, "VESTA 3 for Three-Dimensional Visualization of Crystal, Volumetric and Morphology Data," *Journal of Applied Crystallography* 44 (2011): 1272–1276, https://doi.org/10.1107/S0021889811038970.

72. M. Methfessel and A. T. Paxton, "High-Precision SAMPLING for Brillouin-Zone Integration in Metals," *Physical Review B* 40 (1989): 3616, https://doi.org/10.1103/PhysRevB.40.3616.

73. S. P. Ong, S. Cholia, A. Jain, et al., "The Materials Application Programming Interface (API): A Simple, Flexible and Efficient API for Materials Data Based on Representational State Transfer (REST) Principles," *Computational Materials Science* 97 (2015): 209–215, https://doi.org/10.1016/j.commatsci.2014.10.037.

Supporting Information

Additional supporting information can be found online in the Supporting Information section.

Supporting File: adfm74167-sup-0001-SuppMat.docx.

“Heterogeneous Coherent Interface Enabling Nonstochastic Crystallization for Phase-Change Memory”

Supporting Information

Tian-Yu Zhao, Jiahao Li, Nian-Ke Chen, Bai-Qian Wang, Xiaomin Cheng*, Shun-Yao Qin, Huan-Ran Ding, Shengbai Zhang, Hong-Bo Sun, Xiangshui Miao*, and Xian-Bin Li**

T.-Y. Zhao, N.-K. Chen, B.-Q. Wang, S.-Y. Qin, H.-R. Ding, X.-B. Li
State Key Laboratory of Integrated Optoelectronics, College of Electronic Science and Engineering (College of Integrated Circuits), Jilin University, Changchun 130012, China
E-mail: chennianke@jlu.edu.cn; lixianbin@jlu.edu.cn

J. Li, X. Cheng, X. Miao
School of Integrated Circuits, Hubei Key Laboratory for Advanced Memories, Wuhan National Laboratory for Optoelectronics, Huazhong University of Science and Technology, Wuhan 430074, China
E-mail: xmcheng@hust.edu.cn; miaoxs@hust.edu.cn

S. Zhang
Department of Physics, Applied Physics, and Astronomy, Rensselaer Polytechnic Institute, Troy, NY 12180-3590, USA

H.-B. Sun
State Key Lab of Precision Measurement Technology and Instruments, Department of Precision Instrument, Tsinghua University, Beijing 100084, China

Tian-Yu Zhao and Jiahao Li contributed equally to this work.

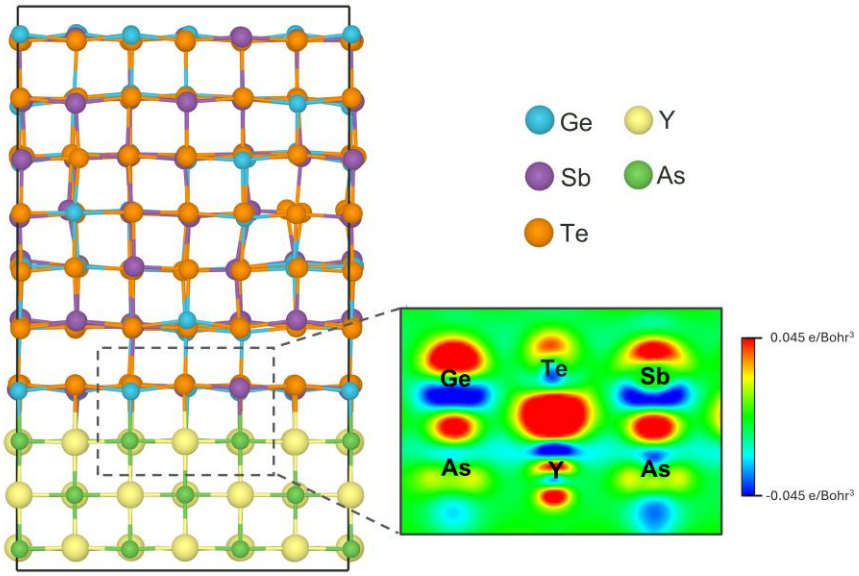

Figure S1. The charge density difference of the YAs/$Ge_2Sb_2Te_5$ coherent interface structure, calculated by subtracting the density distributions of the materials on both sides of the interface from the total density distribution of the structure. In the figure, the regions with positive values represent increases in electron density, while the regions with negative values indicate decreases in electron density.

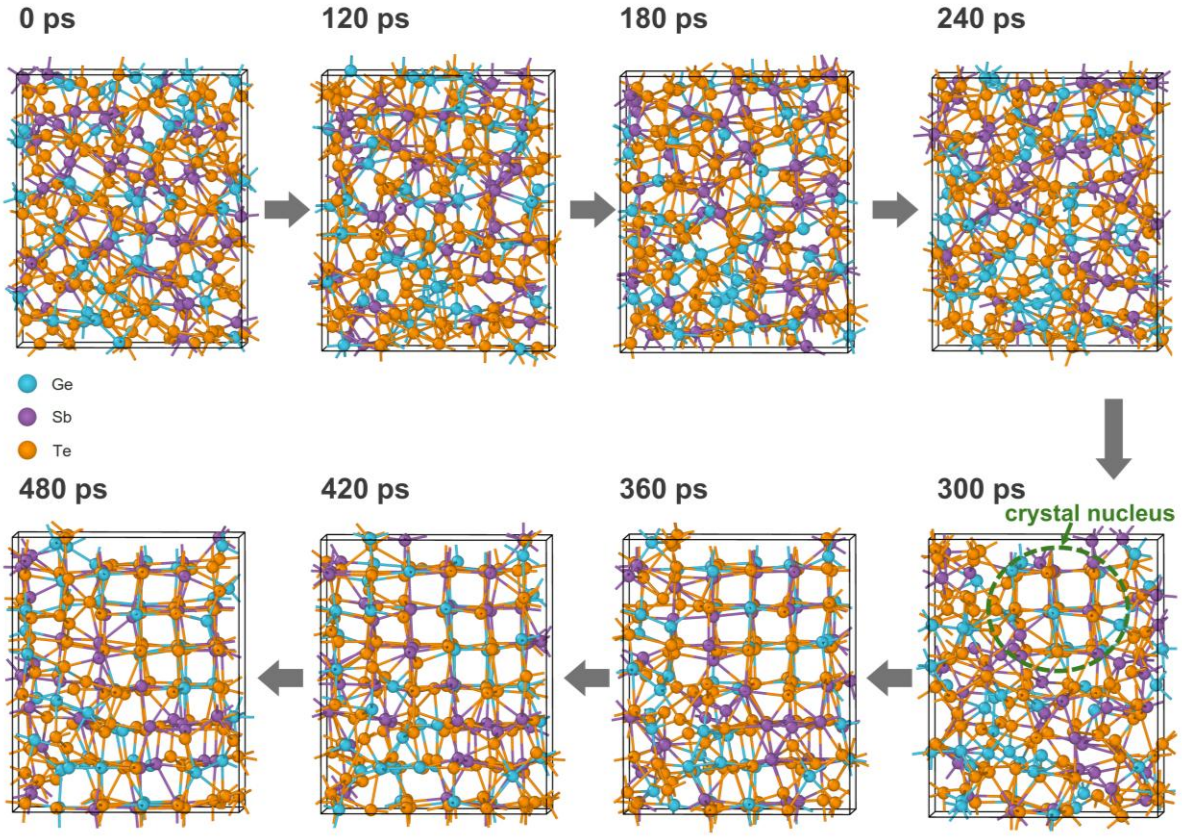

Figure S2. The crystallization process of bulk GST. The random nucleation process is the main part in the entire crystallization. A stable nucleus can only be observed after 300 ps (corresponding to the beginning of stage II in Figure 2c of the main text).

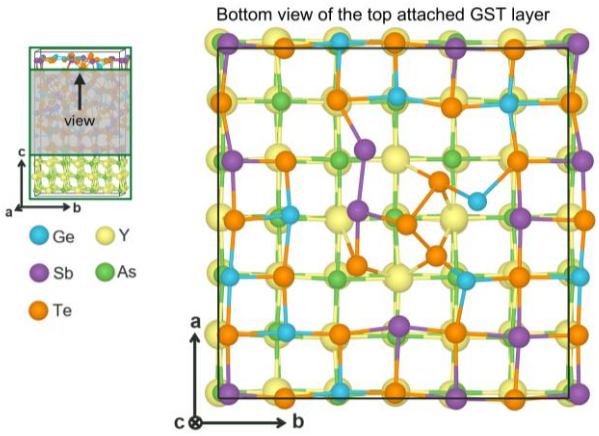

Figure S3. Bottom view of the top GST atomic layer next to YAs in the melt-quenched amorphous YAs-GST structure.

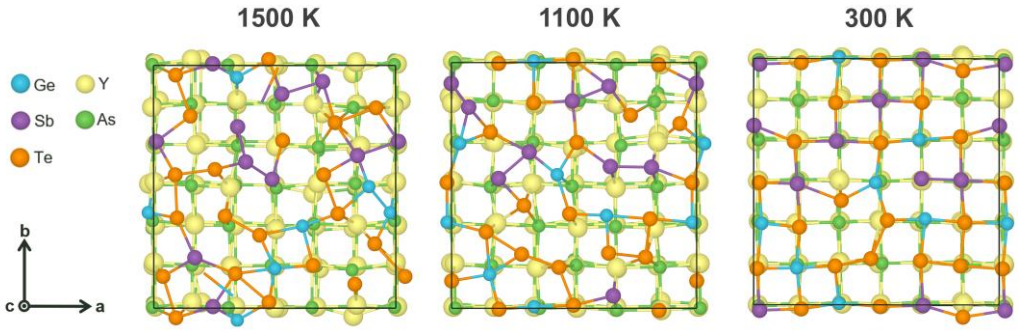

Figure S4. Top view of the GST interfacial layer closely next to YAs in the melting process (1500 K, 1100 K) and the subsequent quenched state (300 K). Here, the structure at 300 K is taken from the one of Figure 3a in the main text for comparison.

Note S1

In this supplementary note, we show the preliminary experimental verification of the acceleration of the SET process. Figure S5a presents a schematic of our via-hole device structure, in which the central layer is the phase-change material. However, YAs has long been neglected by academia and industry, imposing challenges for us to conduct the experiment to directly fabricate the interface structure in the phase change material layer. Due to the unavailability of a pure YAs target at present, we instead use a $Y_{0.3}As_{0.3}Ge_2Sb_2Te_5$ target to sputter the PCM material. The YAs-GST is deposited as a 100-nm-thick layer in the hole with a diameter of 250 nm in the typical hole-type PCM device. Figure S5c demonstrates that the YAs-GST device, prepared with the above-mentioned approach, achieves a SET speed four times faster than that of the pure GST device under even lower operation voltages. Specifically, the YAs-GST device exhibits a SET speed of 20 ns under 1.6 V, compared to 80 ns under 3.8 V for the GST device. The resistance-voltage characteristics of both devices at their fastest SET speed are detailly presented in Figure S5d. Regarding the 'two-step crystallization' behavior observed in the Figure S5d during the SET process, it may reflect two distinct crystallization dynamics: one occurring near the coherent interface and the other possibly in regions far from it. Crystallization adjacent to the coherent interface is expected to proceed more readily, whereas regions farther away rely on self-nucleation of GST, which is comparatively more difficult. Further investigation will be required for better understanding.

However, we note that the improved SET speed shown in the experiment may come from several potential factors. In fact, other heterogeneous rock-salt materials may also spontaneously form because of using a single $Y_{0.3}As_{0.3}Ge_2Sb_2Te_5$ target to sputter the YAs-incorporated-GST material. For example, YSb and YTe also have significantly higher cohesive energies (4.76 eV/atom for YSb and 4.91 eV/atom for YTe) than that of GST (2.85 eV/atom), shown in Figure S5b. Their lattice mismatches with GST are small as well, i.e., 2.36% for YSb and 1.52% for YTe. In other words, the three kinds of coherent interfaces, including YAs/GST, YSb/GST, and YTe/GST, may form in the experiment and facilitate crystallization. In fact, all the three materials including YAs, YSb, and YTe mentioned in Figure S5b bypass the 4 criteria in our high-throughput screening and fall within the 71 candidate materials as shown in Table 1 of the main text.

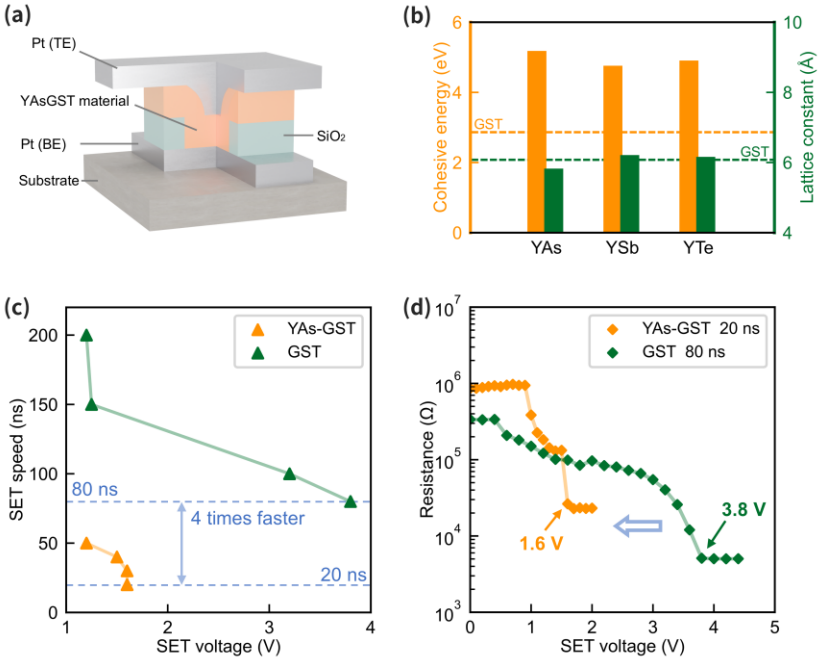

Figure S5. The performance comparison of the SET speed between the device based on YAs-GST and the one based on pure GST. Two kinds of devices have the same structure. a) Schematic of the PCM device. b) Cohesive energy and lattice constant of heterogeneous rock-salt materials, which may form because of using a single $Y_{0.3}As_{0.3}Ge_2Sb_2Te_5$ target to sputter the YAs-incorporated-GST material. All three materials meet the requirements of forming coherent interfaces with GST. c) Voltage dependence of the SET speed for the YAs-GST and pure GST devices. d) The resistance-voltage characteristics of the YAs-GST and pure GST devices under their shortest SET pulses (20 ns vs. 80 ns).

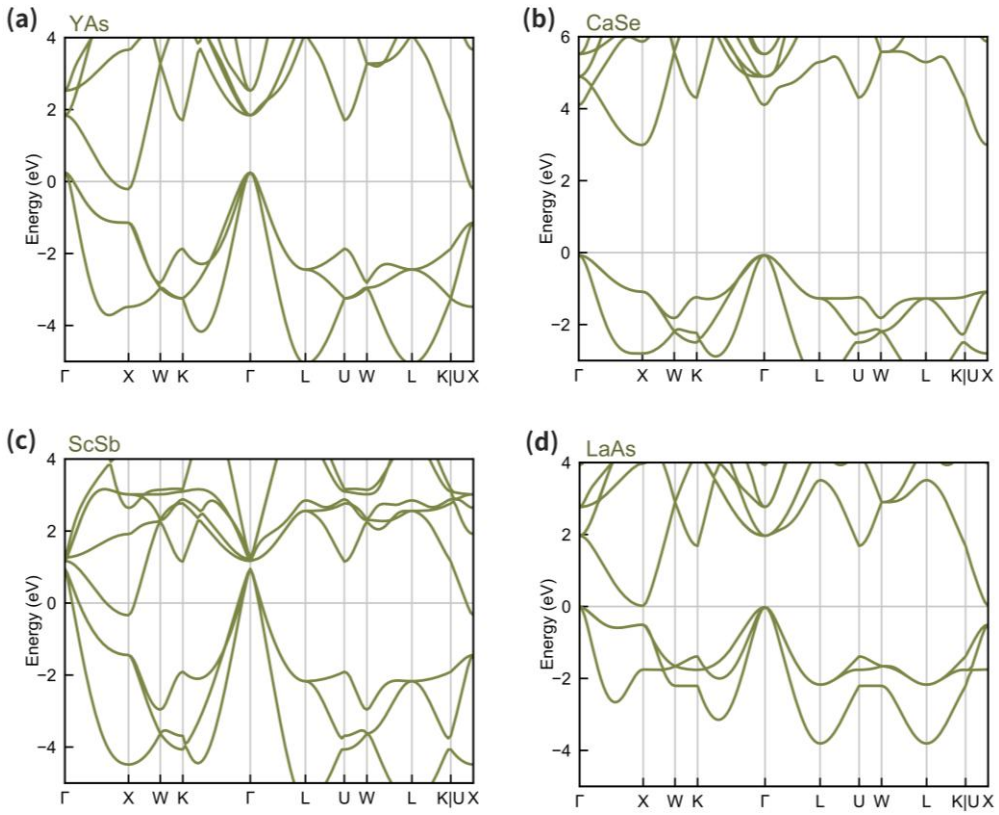

Figure S6. The band structures of four typical candidate rock-salt materials calculated with the HSE functional. Among them, YAs, ScSb, and LaAs exhibit semi metallic band structures, whereas CaSe shows a clear band gap.

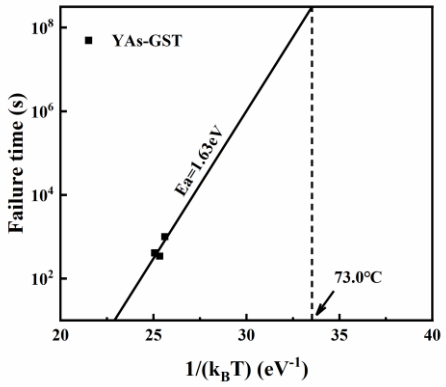

Figure S7. Ten-year data retention evaluation of YAs-incorporated GST material.

Note S2

To verify the robustness of the coherent interface strategy, we perform AIMD simulations using ScSb, which is an extra candidate of the high-throughput screening. Figure S8 shows the snapshots of the ScSb/GST model during the recrystallization. Similar to the case of YAs/GST, the amorphous GST rapidly recrystallized via the growth from the coherent interface.

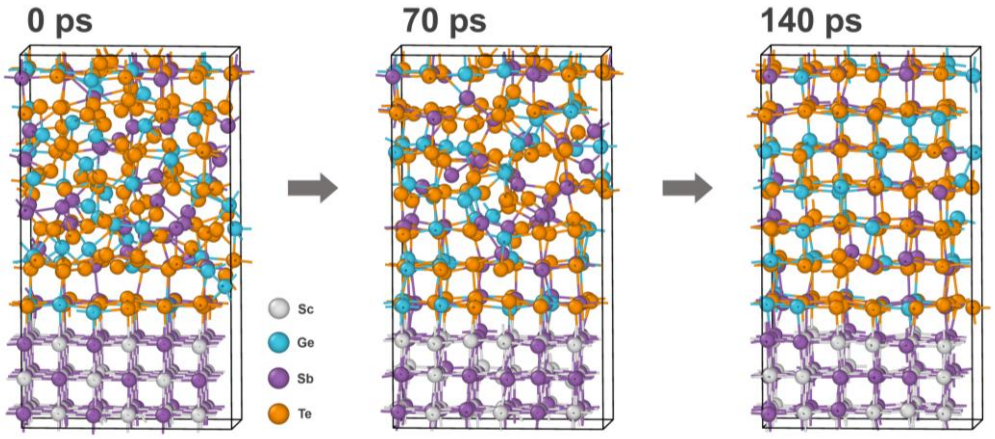

Figure S8. Rapid crystallization process of GST in coherent interface structures formed between ScSb and GST.

Table S1. 14 easily-formed candidates further screened from the 71 candidates in Table 1. In the table, mp-id represents the material ID in the Materials Project database. E_{hull} represents the energy above hull. E_c represents the cohesive energy. Lattice constants are also displayed.

mp-id	Formula	E_{hull} (eV/atom)	Lattice constant (Å)	E_c (eV/atom)
mp-1415	CaSe	0	5.942	4.578
mp-2563	CeSe	0	6.043	5.789
mp-20587	EuS	0	5.884	4.976
mp-510404	GdSe	0	5.825	5.349
mp-2350	LaS	0	5.885	6.168
mp-1161	LaSe	0	6.104	5.724
mp-1453	NdSe	0	5.975	5.713
mp-627	NpSe	0	5.850	5.366
mp-1232234	PmSe	0	5.922	5.699
mp-2495	PrS	0	5.809	6.183
mp-1674	PrSe	0	6.029	5.729
mp-2288	PuSe	0	5.886	4.921
mp-1447	SmSe	0	5.888	5.662
mp-1561	TbSe	0	5.769	5.556